Journal of Power Sources 195 (2010) 7943–7958

Contents lists available at ScienceDirect

Journal of Power Sources

journal homepage: www.elsevier.com/locate/jpowsour

Characterization and analysis methods for the examination of the heterogeneous solid oxide fuel cell electrode microstructure: Part 2. Quantitative measurement of the microstructure and contributions to transport losses

Kyle N. Grew, Aldo A. Peracchio, Wilson K.S. Chiu*

Department of Mechanical Engineering, University of Connecticut, 191 Auditorium Rd., Storrs, CT 06269-3139, United States

ARTICLE INFO

Article history:
Received 1 April 2010
Received in revised form 2 July 2010
Accepted 5 July 2010
Available online 3 August 2010

Keywords:
Microstructure
X-ray
Lattice Boltzmann
Transport

ABSTRACT

Advanced characterization and analysis of multifunctional materials, such as the materials found in heterogeneous solid oxide fuel cell (SOFC) electrode architectures, can help to provide a qualitative and quantitative understanding of how these structures respond to different manufacturing and operating practices. Dense, opaque materials, which have large X-ray mass absorption coefficients and features on sub-micrometer length scales, can make characterization difficult. Advances in tomographic X-ray imaging can permit this level of detailed characterization, and complement stereographic scanning electron microscope measurements that have also been reported. In this second part of a two-part study, details regarding quantitative characterization methods that have been used to examine the SOFC anode microstructure are reported. The detailed formulation and validation of a phase size distributions for the three constitutive phases, as well as resistive loss microstructure-induced resistive loss distributions in the nickel (Ni) and yttria-stabilized zirconia (YSZ) phases are provided in this section.

1. Introduction

Advances in X-ray and electron based imaging methods have provided new capabilities for imaging and reconstructing dense and opaque 3-D heterogeneous structures at spatial resolutions on the order of tens of nanometers in length. Demonstrations of these capabilities include tomographic reconstruction using a full-field transmission X-ray microscope (TXM), or X-ray computed tomography (XCT), as have previously been demonstrated by the authors and coworkers [1,2]. These capabilities may include the use of stereographic methods in which a focused ion beam is used in conjunction with a scanning electron microscope (FIB-SEM) to ascertain the 3-D nanostructure, as reported by independent groups [3–6].

These methods enable the digital reconstruction of the details of the heterogeneous nano/microstructure. Exploitation of the elemental X-ray absorption edges has recently been demonstrated for the elemental phase mapping of the SOFC anode microstructure [1]. Similar capabilities are available for the FIB-SEM measurement, due to contrast differences in back-scattered electrons coming from materials of different atomic masses [3–6]. The XCT and FIB-SEM methods can be viewed as complementary methods, where each offers unique opportunities and capabilities.

This study is motivated by interests in advancing the understanding of nano- to micro-structured heterogeneous materials and their functional impact on devices like the SOFC through advanced characterization methods [7,8]. Developments in the understanding of these materials and structures should help us to address their limitations and degradation mechanisms while enhancing their functionality. The XCT and FIB-SEM characterization methods can enable new degrees of scientific and engineering insight into the materials and structures used in these systems. The scientific understanding of the nano/microstructures imaged using these methods can also be used for advanced modeling and simulation.

The details regarding the formulation, methods, validation, and implications of several quantitative characterization and analysis methods are presented in this work. These are methods that the authors have used to characterize the porous Ni–YSZ cermet SOFC anode in previous studies [1,2,9,10]. Part 1 of this effort [7] describes the details of methods that are used to calculate the volume fraction, contiguity, tortuosity, and interfaces of the pore, Ni, and YSZ phases in these structures. Here, a detailed look at methods used by the authors to investigate the size distribution of these same phases and their effect on transport is provided. This begins with the development of a phase size distribution, which is used to provide the relative volumetric contributions of unique characteristic diameters of the individual phases in the structure. The effects that these phase structures have on transport are provided with a resistive loss and microstructure-induced resistive loss distributions. This requires a transport phenomena study, which is

* Corresponding author. Tel.: +1 860 486 3647; fax: +1 860 486 5088.
E-mail address: wchiu@engr.uconn.edu (W.K.S. Chiu).

0378-7753/$ – see front matter © 2010 Elsevier B.V. All rights reserved.
doi:10.1016/j.jpowsour.2010.07.006

Table 1
Properties of generated phenomenological structure and grid.

Set	Phase	Volume fraction	Set particle diameter, μm	Particles	Voxel size, nm³	Voxels/edge	Volume, μm³
1	Ni	0.330	1.0	95	50^3	–	–
	YSZ	0.329	1.0	165	50^3	–	–
	Pore	0.341	NA	–	50^3	–	–
	Volume	1.00	NA	–	50^3	100	5^3
2	Ni	0.347	1.0	100	50^3	–	–
	YSZ	0.336	0.5	1400	50^3	–	–
	Pore	0.317	NA	–	50^3	–	–
	Volume	1.00	NA	–	50^3	100	5^3
3	Ni	0.336	0.5	800	50^3	–	–
	YSZ	0.331	1.0	175	50^3	–	–
	Pore	0.333	NA	NA	50^3	–	–
	Volume	1.00	NA	–	50^3	100	5^3

performed with a lattice Boltzmann method. The demonstrations of the resistive loss distributions are demonstrated solely in the YSZ phase in this study at this time; however, they can be extended to the other phases. This goal of this manuscript is to relay the details of the development, verification, and validation of the methods that the authors have performed to quantitatively study the details of the heterogeneous structure to the community. These methods are described in the context of the SOFC porous Ni–YSZ anode structure, imaged using XCT methods [1,2,11–13]. The results and discussion presented in this work take the form of the verification and validation of the described methods along with discussions of these studies and their implications.

2. Samples and structures

In Part 1 of this study, details are provided regarding a number of unique samples and data sets [7]. These data sets include (i) a sample of a porous Ni–YSZ SOFC anode imaged and reconstructed using tomographic methods with elemental mapping via subsequent scanning across the elemental X-ray absorption edges in a TXM with a synchrotron source, (ii) two samples of independent porous Ni–YSZ anodes imaged and reconstructed with a commercial XCT system with a laboratory source, and (iii) samples that have been artificially generated using Monte-Carlo, or sphere-packing, methods. These same samples and generated structures are considered in this study.

The discussion in Part 1 includes details that pertain to the sample preparation and references for the methods used. The sphere-packing samples are not considered as being representative of the SOFC anode. Rather, they are generated as phenomenological cases that can aide in the development and testing of the methods discussed in both parts of this study. Table 1 provides a description of the structures and constituent particle sizes that are considered in this work. This includes structures that were not considered in Part 1. A complete review of these samples, data sets, and methods are not repeated here. Those interested are referred to Part 1 [7] and several studies detailing the use of XCT and X-ray imaging efforts [1,2,11,13,14].

3. Quantitative characterization methods

3.1. Phase size distribution (PSD)

To examine the phase-specific, volumetric dependence of the sample morphology, a method which resembles a ray-shooting method has been developed. This method is used to identify a phase size distribution, which describes the Ni, YSZ, and pore regions of the sample structures. The phase size distribution, provides the contribution of a specific phase diameter, D, within the detailed, phase-specific structure to the total volume fraction which that phase occupies. This diameter may be thought of as related to the cross-sectional area of a region of a given phase (i.e., $D \propto \sqrt{A}$).

3.1.1. Lattice Boltzmann discretized ray-shooting method

The ray-shooting method developed in this study is built upon the 3-D, 19-velocity vector lattice Boltzmann method (LBM) discretization scheme [15,16]. Each voxel has a set of inter-connecting vectors that corresponds to 18 directions surrounding the local zero position at the center of the voxel. This provides a set of self-consistent direction vectors that discretize the geometric domain. This discretization is used to simplify the analysis of the digital structure by limiting the directions that are considered.

The 19-direction vectors of the LBM discretization lie at and inter-connect every voxel within the structure. Voxels that lie at the phase interface are of specific interest. Each of these interfaces serves as a launch point for a single ray. The ray is launched in the normal direction from this interface, corresponding to one of the 19-direction vectors in the LBM discretization. The ray is propagates along one of these direction vectors until a second phase is reached within the geometry file, providing a ray length. The geometric file is iteratively searched for phase interfaces and continues until the entire structure has been examined. The lengths of individual rays are appended to a file for post-processing as they are identified. Additional details of the tabulation of the ray lengths and several sample scenarios are provided in Ref. [1].

Several intricacies of the ray-shooting method require discussion. In a separate effort [1], several hypothetical cases were shown. A similar hypothetical cross-section is shown in Fig. 1. We ignore the scalar resistive loss values, Q, in the individual voxels in this representation in this discussion. For the case in Fig. 1, rays would be launched from each square interface, totaling 12 rays of 3 voxels and 4 rays of $3\sqrt{2}$ from the corners. The number of rays identified for a given cross-section may vary from a larger or smaller cross-section and would propagate down the length of the phase.

3.1.2. Analytic development

To interpret the data collected by the ray-shooting method, an analytic development is needed. This development permits a quantitative description of the sample's microstructure on the basis of the tabulated ray-shooting data. A unique method is developed here. This method provides quantitative descriptions of the microstructure that are similar to those identified in the mercury intrusion porosimetry (MIP) development in Part 1 (e.g., $\langle V_{\text{Pore}}/V_T \rangle$ and α_n) [7]. A benefit of the new development is that it provides the additional flexibility to interrogate the dense phases of the sample (i.e., Ni and YSZ) because of the digital representation of the structure.

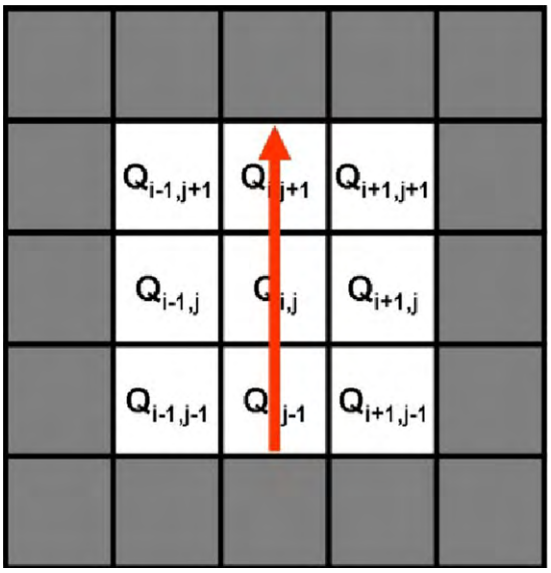

Fig. 1. A 2-D representation of the ray-shooting method used to analyze the resistive loss distribution within the sample. Scalar values of the net joule heating populating individual voxels. The ray length and average joule heating of the voxels traversed are coherently examined.

A phase size distribution (PSD) function is defined for this development. This PSD is representative of the ratio of the volume of a given phase at a particular phase diameter, D, within a differential diameter bin width, ΔD, relative to the total sample volume. It describes the relative volumetric composition of the individual phases within the sample. There is a careful distinction between these PSDs and those formulated using MIP. These two methods address the sample structure from different perspectives. Both methods have their own merits, benefits, and deficiencies, and should be viewed as complementary but unique. This topic will be elaborated upon in the discussion.

Returning to the development of a PSD, the lengths tabulated by the ray-shooting method are in the form of a column, $\left[N_l^{\text{Voxels}}\right]$, where N_l^{Voxels} is the number of unit voxels that are traversed by ray, l. This column is provided in as a series of double precision, irrational numbers and can be converted to physical lengths by multiplying by the unit voxel length. These ray lengths are characteristic of the structure and are proportional to the cross-sectional area of the phase path (i.e., $D \propto \sqrt{A}$). They are considered and described as phase path diameters, D, in this description.

Several assumptions are required to take this set of diameters to form a PSD. To form the PSD, it is assumed that phase paths that provided the diameters are predominately continuous through the structure, independent, and do not experience sudden and large changes in cross-section. The diameters that have been gathered from the detailed structure can be used to define a histogram, $N(D_i,\Delta D)$, that delimitates the number of rays, $\eta(D_i,\Delta D)$, in a bin of diameter, D_i, within a differential diameter, ΔD, that corresponds to the histogram bin width. The representation of an individual bin of diameter, i, within a differential diameter, ΔD, is denoted by the quantities in parenthesis from here on (i.e., $(D_i,\Delta D)$). Equal bin widths, ΔD, are used over a single histogram. The histogram representing the number of rays, $N(D_i,\Delta D)$, is defined,

$$N(D_i, \Delta D) = \frac{\eta(D_i, \Delta D)}{\Delta D} \tag{1}$$

where the distribution function $N(D_i,\Delta D)$ has units of inverse length (e.g., μm^{-1}). The total number of rays in all bins, $\hat{\eta}$, is obtained by integrating over all diameters,

$$\hat{\eta} = \int N(D)\, dD = \sum_{i=1}^{\text{M-bins}} N(D_i, \Delta D)\Delta D \tag{2}$$

as is shown for both a continuous function and the piecewise histogram containing M-bins. This assumes that a piecewise representation of the continuous function is valid.

The number of rays per unit voxel length of centerline, $N_{\text{Rays}}^{\text{C.L.}}$, for a phase path of a given diameter is needed. Because the cubic representation of the real structure is implicit, the number of rays per unit voxel centerline is correlated to the perimeter of the phase cross-sections for a given path,

$$N_{\text{Rays}}^{\text{C.L.}} = \frac{P}{\delta} + 4 \approx C_o\left(\frac{D}{\delta} + 1\right) \tag{3}$$

where P is the phase path perimeter, δ is the unit voxel length, and 4 is a geometric constant that arises due to the cubic representation of the structure. A geometric constant of proportionality, C_o, is required to scale the quantity in Eq. (3). For square cross-sections, this constant takes on the value of $C_o \approx 4$. This geometric constant requires generalization to represent any number of shapes of phase cross-sections which can exist in the real structure. Using inspection, typical number weighted mean diameters values for this constant range between 3 and 5 for any number of geometric cross-sectional shapes that are constructed on a cubic lattice. This provides qualitative support for using this geometric constant as a constant of integration to normalize the data, as will be described later in this development.

Eq. (3) may now be extended to describe the number of rays that would exist for an individual phase path traversing the sample structure,

$$N_{\text{Rays}}^{\phi} \approx C_o\left(\frac{D}{\delta} + 1\right)\tau_\phi k \tag{4}$$

where τ_ϕ is the tortuosity of the phase path and k is the number of voxels per edge of the cubic structure. Eq. (4) assumes that the phase path maintains a diameter, D, and a tortuosity that is representative of the phase within the sample.

The number of phase paths in the sample structure that correspond to bin $(D_i,\Delta D)$ can be found by taking the ratio of the total number of rays in bin $(D_i,\Delta D)$ to the number of rays associated with the phase path of that diameter (Eq. (4)).

$$\zeta(D_i, \Delta D) = \frac{1}{C_o}\frac{N(D_i, \Delta D)\Delta D}{((D_i/\delta) + 1)\tau_\phi k} \tag{5}$$

This quantity is useful, but difficult to interpret. Therefore, the volume associated with an individual phase path, $V_i^{\phi}(D_i)$, is approximated,

$$V_i^{\phi}(D_i) = C_1(D_i)^2\tau_\phi k\delta \tag{6}$$

where C_1 is a second geometric constant that is used to generalize the relationship between the diameter and cross-sectional area. For a path with a square cross-section, it will take on the value $C_1 \approx 1$.

Multiplying the volume associated with a phase path (Eq. (5)) by the number of phase paths that fall within $(D_i,\Delta D)$ (Eq. (6)), the total volume in the associated phase paths is,

$$\Delta V_i^{\phi}(D_i, \Delta D) = \zeta(D_i, \Delta D)V_i^{\phi} = C^*\frac{N(D_i, \Delta D)(D_i)^2\Delta D}{(D_i/\delta) + 1}\delta \tag{7}$$

where $C^* = C_1/C_o$. This function is normalized by the total sample volume considered, $V_T = (k\delta)^3$, and subsequently divided by the differential bin diameter to form a distribution function.

$$\frac{\Delta V_i^{\phi}(D_i, \Delta D)}{V_T} = \frac{\Delta V_i^{\phi}(D_i, \Delta D)}{(k\delta)^3} = C^*\frac{N(D_i, \Delta D)(D_i)^2\Delta D}{(D_i/\delta) + 1}\frac{\delta}{(k\delta)^3} \tag{8}$$

$$\alpha_n(D_i, \Delta D) = \frac{\Delta V_i^{\phi}(D_i, \Delta D)/V_T}{\Delta D} = C^* \frac{N(D_i, \Delta D)(D_i)^2}{(D_i/\delta)+1} \frac{\delta}{(k\delta)^3} \quad (9)$$

The normalized PSD, $\alpha_n(D_i,\Delta D)$, represents the volume fraction of all of the phase paths contained in $(D_i,\Delta D)$. This distribution has units of inverse length (i.e., μm^{-1}) and C^* is a combined geometric constant. It will take on the value of $C^* \approx 1/4$ for square cross-sections.

This geometric constant, C^*, can be generalized for all shapes. Integrating $\alpha_n(D_i,\Delta D)$ over all diameters, should provide the phase volume fraction, $\langle V_\phi/V_T \rangle$.

$$\langle V_\phi/V_T \rangle = \int \alpha_n(D)\, dD = \sum \alpha_n(D_i, \Delta D)\Delta D \quad (10)$$

Substituting Eq. (9) into Eq. (10), we find an expression for C^* in terms of $\langle V_\phi/V_T \rangle$.

$$C^* = \langle V_\phi/V_T \rangle \frac{\delta}{(k\delta)^3} \frac{1}{\sum_{j=1}^{\text{M-bins}} \left[(N(D_j, \Delta D)(D_j)^2/((D_j/\delta)+1))\Delta D\right]} \quad (11)$$

Inserting Eq. (11) into Eq. (9), yields a normalized phase size distribution.

$$\alpha_n(D_i, \Delta D) = \frac{\langle V_\phi/V_T \rangle}{\sum_{j=1}^{\text{M-bins}} \left[(N(D_j, \Delta D)(D_j)^2/((D_j/\delta)+1))\Delta D\right]} \times \frac{N(D_i, \Delta D)(D_i)^2}{(D_i/\delta)+1} \quad (12)$$

Two salient features can be noted in the examination of the PSD in Eq. (12). This distribution can be integrated, as provided in Eq. (13), in a continuous piecewise manner. The relative volume fraction of the phase attributed to regions characterized by a diameter, D, and smaller is the result.

$$\langle V_\phi/V_T \rangle\Big|_0^D = \int_0^D \alpha_n(D)\, dD = \sum_0^{\text{Bin-L}} \alpha_n(D_i, \Delta D)\Delta D \quad (13)$$

A normalized form may also be used, to present the percentage of the total volume contained at diameter, D, and smaller was shown. The second feature that may be recognized is that for all of the complexity that is present in Eq. (12), the method is still built upon a simplified geometric construct. Therefore, the integrity of the method and underlying assumptions can be checked by the comparison of the normalization constant, C^*, to that used during the theoretical development, $C^* \approx 1/4$.

3.2. Transport phenomena

A requisite analysis of transport phenomena is performed for this study so that correlations between transport processes and the quantitative microstructural characterization can be completed. The lattice Boltzmann method (LBM) provides a convenient framework for the examination of the transport processes in the heterogeneous electrode structure. LBM has the ability to capture the appropriate physics, is amenable to complex geometric structures, and uses of a regular mesh with high grid independence [17–29]. Detailed reviews on the governing theory and implementation, boundary conditions, and parallel scalability are widely available in the literature [17–29]. The implementation in this study resembles those reported in previous studies [10,27,30,31], with the consideration of a second order zero flux boundary condition at the impermeable phase interfaces [19,32].

The extension of the LBM theory and methodology for the consideration of the charge transfer processes in the Ni and YSZ regions is completed using an analogy, and on the basis of the ability of the LBM algorithm to recover a solution to Laplace's equation when evaluating binary molar mass transfer in the absence of viscous flow [27]. Charge transfer solutions are scaled using analogous non-dimensional groups to those used for mass transport in past studies [10,27,31]. In this study, we focus on transport in YSZ; however, the methods are also amenable to mass transfer and electronic charge transfer.

The LBM studies used in this work are performed on an SGI Altix 3700. Parallelization is completed using a vertical domain decomposition scheme. Inter-processor communications are treated using the message passing interface. Solutions for the transport processes are examined under steady-state conditions. Convergence of the steady-state solution is monitored using the total and species conservation principles. Solutions are considered when converged and the error in the species balance was less than 0.1%.

Post-processing of the results is required to identify the resistive losses due to joule heating and display the scalar field associated with these losses in finite regions of the structure. This analysis is accomplished by using the flux outputs from the LBM analysis at each voxel within the structure. The net joule heating in a finite voxel at a position (i,j,k) can be described as,

$$Q'''(i,j,k) = \rho\left[i_x(i,j,k)^2 + i_y(i,j,k)^2 + i_z(i,j,k)^2\right] \quad (14)$$

where $Q'''(i,j,k)$ is the heat liberated per unit volume at a given voxel position (i,j,k), ρ is the material's resistivity, and $i_x(i,j,k)$ is the current density in the x-direction as the corresponding voxel location. The heat release, Q''', can be evaluated on a per unit sample volume or per unit phase volume basis. The net heat release at position (i,j,k) in terms of the net heat released, or absolute value, can also be shown as,

$$Q(i,j,k) = Q'''(i,j,k)\, dV \quad (15)$$

and is also of use. In this form, dV is the finite voxel volume.

Using the scalar representation of these heat release quantities, they are written to a file that mirrors the geometric structural file for subsequent analysis. This file maintains a scalar heat release quantity at each voxel, representative of the heat release over that voxel volume. Separate files are constructed using the both the net heat release and that specific to the volume of the voxel. These files are used in subsequent sections.

3.3. Resistive loss and microstructure-induced resistive loss distributions

Using the transport analysis data files discussed in Section 3.2, the scalar resistive loss values can be examined in a complementary manner to the geometric structures in the geometry files. A conceptual representation of this file containing resistive loss values is shown in Fig. 1, where a phenomenological 2-D cross-section is shown. In Fig. 1, a representative ray is shown in a structure that is identical to the structure of the geometry file, which was used to analyze the PSDs of these regions in Section 3.1. However, in Fig. 1, additional information concerning the resistive losses existing in each of the voxels that are traversed is available. This provides the ability to *coherently* examine and interpret the detailed geometry and the associated resistive losses. The end result of this development is the formation of a resistive loss distribution (RLD). The resistive losses in this distribution are those that arise from Joule heating.

An elaboration upon its physical interpretation and implication on our understanding of the heterogeneous SOFC electrode microstructure is merited prior to detailing the methods used to perform this analysis. It is well understood that any attempt

to force a large current through a narrow region can result in increased resistive losses due to joule heating. This represents the irreversibility, or entropy generation, attributed to the charge transfer processes. This irreversibility can be especially problematic in structures that are not composed of materials that are ideal conductors due to an increased resistivity. The same goes for regions with geometric constrictions, or regions of reduced cross-section. In the heterogeneous structures that are representative of the SOFC anode, the implication and effects of the phase-network are difficult to interpret. Underlying these difficulties is an insufficient understanding of the details of the heterogeneous structures themselves. Interpretations of the phase structure can aid this understanding, but the full impact of the phase structure is not known without discrete analysis. To better appreciate and quantify the connections between the structural features within the heterogeneous phase structure and the resulting irreversibility, some unifying quantitative analysis is required.

A method that is capable of identifying correlations between the joule heating losses and the detailed phase structure can provide some considerable insights. The ray-shooting method used in Section 3.1 provides a useful framework. By utilizing this method, a consistent description of the phase diameter is provided while also allowing the examination of a complementary structure detailing the joule heating losses, as is demonstrated in Fig. 1.

3.3.1. Resistive loss ray-shooting methods

Some additional clarification of the use of the ray-shooting method to examine resistive losses is necessary before any data can be examined. In Section 3.1, the ray-shooting process is described in detail. Here, an additional ray is shot in the complementary joule heating data structure in this analysis. This ray and has the exact same launch and termination points as the one used to examine the geometric structure. In the resistive loss structure, the resistive losses in each individual voxel are summed as the ray traverses this structure. This permits an *average* resistive loss for each ray to be calculated.

$$\overline{q'''}_l = \frac{1}{N_l^{\text{Voxels}}} \sum_{\text{path-l}} q'''(i,j,k) \tag{16}$$

In Eq. (16), $\overline{q'''_l}$ is the average joule heating per unit volume for ray-l, with a ray length of N_l^{Voxels}. The full geometric and joule heating data files are examined in a coordinated manner. A two-column table is generated to record the values of the number of voxels traversed by each ray and the complementary average joule heating recognized for that ray (i.e., $\left[N_l^{\text{Voxels}}, \overline{q'''_l}\right]$). This table provides the data which is used with the remainder of this development.

3.3.2. Analytic development

The table of the complementary ray lengths and average joule heating values are concurrently examined to interpret the data collected with the ray-shooting method. When the ray lengths, or diameters, are broken down into the histogram $N(D_i, \Delta D)$ (i.e., Eq. (1)), the *average* joule heating values associated with these same rays are concurrently *summed* for these corresponding rays in bin $(D_i, \Delta D)$. This permits the sum of the average joule heating values for the bin to be averaged a second time, using the number of rays falling in the same bin for the ray lengths, $\eta(D_i, \Delta D)$.

$$\gamma(D_i, \Delta D) = \frac{\sum_l \overline{q_l'''}\big|_{D_i, \Delta D}}{\eta(D_i, \Delta D)} \tag{17}$$

The average joule heating in the phase's structure, $\gamma(D_i, \Delta D)$, is in (W m^{-3}). This representation makes it a property of the detailed structure.

As in Section 3.1.2, a formal distribution function, $\Gamma(D_i, \Delta D)$, is formed by dividing Eq. (17) by the differential bin width, ΔD. This distribution function is representative of the net volumetric joule heating in all phase paths in the structure corresponding to $(D_i, \Delta D)$. This distribution function has a great deal of merit in its own right; however, it is of benefit to link this manipulation back to both the structure and initial transport analysis. It is operated upon by the net volume that was determined for these same phase paths, using the tools developed in Section 3.1. In Eq. (7), the volume of all phase paths in the sample volume is defined. Combining $\Gamma(D_i, \Delta D)$ with Eq. (7), a new distribution function is formed. This distribution function is representative of the net joule heating, in W μm^{-1}, within the structure.

$$\chi_n(D_i, \Delta D) = \Gamma(D_i, \Delta D)\Delta V_\phi(D_i, \Delta D) = \frac{\delta}{C_o \Delta D} \frac{\gamma(D_i, \Delta D)(D_i)^2}{(D_i/\delta)+1} \tag{18}$$

The integration of this distribution function over all differential diameters results in the net joule heating.

$$Q_{\text{net}} = \int_0^\infty \chi_n(D)\, dD \approx \sum \chi_n(D_i/\delta) + 1 \Delta D \tag{19}$$

In Eq. (19), Q_{net} is the net joule heating in the volume, in W. This provides a framework for determining the integration constant, C_o, and resistive loss distribution, $\chi_n(D_i/\delta)+1$.

$$C_o = \frac{\delta}{Q_{\text{net}}} \sum_{j=1}^{\text{M-bins}} \left[\frac{\gamma(D_j, \Delta D)(D_j)^2}{(D_j/\delta)+1} \right] \tag{20}$$

$$\chi_n(D_j, \Delta D) = \frac{Q_{\text{net}}}{\Delta D \sum_{j=1}^{\text{M-bins}} \left[\gamma(D_j, \Delta D)(D_j)^2/((D_j/\delta)+1)\right]} \times \frac{\gamma(D_i, \Delta D)(D_i)^2}{(D_j/\delta)+1} \tag{21}$$

The geometric constant in Eq. (20) is evaluated as a function of the net joule heating in the system. This provides an intuitive normalization based upon that developed for the phase size distribution. The final resistive loss distribution, $\chi_n(D_i, \Delta D)$, permits the explicit connection between two independent analyses (i.e., the PSD and transport phenomena). It combines the two analysis to provide a quantitative measure of the relative volume associated with a given phase diameter in conjunction with its net contribution to the resistive, or joule heating, losses.

As with the PSD, a cumulative form of the resistive losses in Eq. (21) can be shown. Integrating the resistive loss distribution functions with respect to the differential diameter, ΔD, from a zero to a diameter, D, a cumulative distribution is formed. This function represents the net joule heating hat resulted occurred in regions of phase diameters, D, and smaller.

$$Q_{\text{cum}}\big|_0^D = \int_0^D \chi_n(D)\, dD = \sum_0^{\text{Bin-L}} \chi_n(D_i, \Delta D)\Delta D \tag{22}$$

3.3.3. Microstructure-induced resistive loss distribution (MRD)

A final development is a microstructure-induced resistive loss distribution (MRD). Direct comparison of the effects of the structure on the transport losses is difficult in materials like the porous SOFC electrode, which has materials (i.e., pore, Ni, and YSZ) with significantly different transport coefficients. A normalization which accounts for the bulk resistivity of the respective phases/processes is merited for direct comparison. By normalizing these distributions, the direct quantitative comparison of the

nano/microstructure's contributions to resistive losses in the heterogeneous sample structure is permitted.

To do so, the RLD is normalized for the resistive effects attributed to the bulk materials, structures, and conditions. This is achieved by dividing Eq. (21) by the resistive losses attributed to a bulk region of the phase being considered at comparable conditions to isolate the nano/microstructural contributions to the losses. The resistive losses attributed to bulk regions of the considered phase ϕ, are defined as the product of the domain volume V_T, square of the superficial current density i_{cell}, which is also referred to as the operation current density, and the bulk material resistivity, ρ_ϕ. This provides the MRD, which descries the resistive losses induced by the microstructure.

$$\Omega_n^*(D_i, \Delta D) = \frac{\chi_n(D_i, \Delta D)}{\rho_\phi {i_{cell}}^2 V_T} \tag{23}$$

The MRD, $\Omega_n^*(D_i, \Delta D)$, takes on the units of inverse length, μm^{-1}.

4. Results and discussion

4.1. Phase size distributions (PSD)

Ray-shooting methods have been used in several studies to form phase size distributions for quantitatively examining details of the pore, Ni, and YSZ regions of reconstructed sample microstructures [1,2]. We will provide additional details with regard to these results, their verification/validation, and their interpretation. Some independent analysis is also provided in this discussion.

4.1.1. Test structures

This discussion begins with the examination of four simplified structures, which have been generated to demonstrate specific aspects of these methods. These structures serve as simplified checks of the approach. They are intended to support the discussion of the methods developed and are used to verify the numeric methods and assumptions. These structures are rendered in Fig. 2, where they are provided along with their respective PSD. These structures may provide reasonable interpretations of regions within actual samples but do not maintain the same complexity and are therefore easier to see direct comparison between the structures and the PSDs. They are constructed using a 20^3 voxel lattice, which is taken as a 2^3 μm^3 volume making the edge length of an individual voxel, $\delta \approx 100.5$ nm. The phase size distributions are provided with the structural renderings in Fig. 2, which are calculated using Eq. (12), for the structures.

Three observations are made from this analysis. First, the prominent phase diameters are clearly visible. These primary diameters were set during the generation of the structures and each is circled in the appropriate subfigures. The agreement demonstrates the method's ability to capture the primary features of these structures. Second, there is some broadening of the distribution near the base of the primary peaks. This broadening is due to the voxel representation, discrete direction vectors, and the number of bins used to

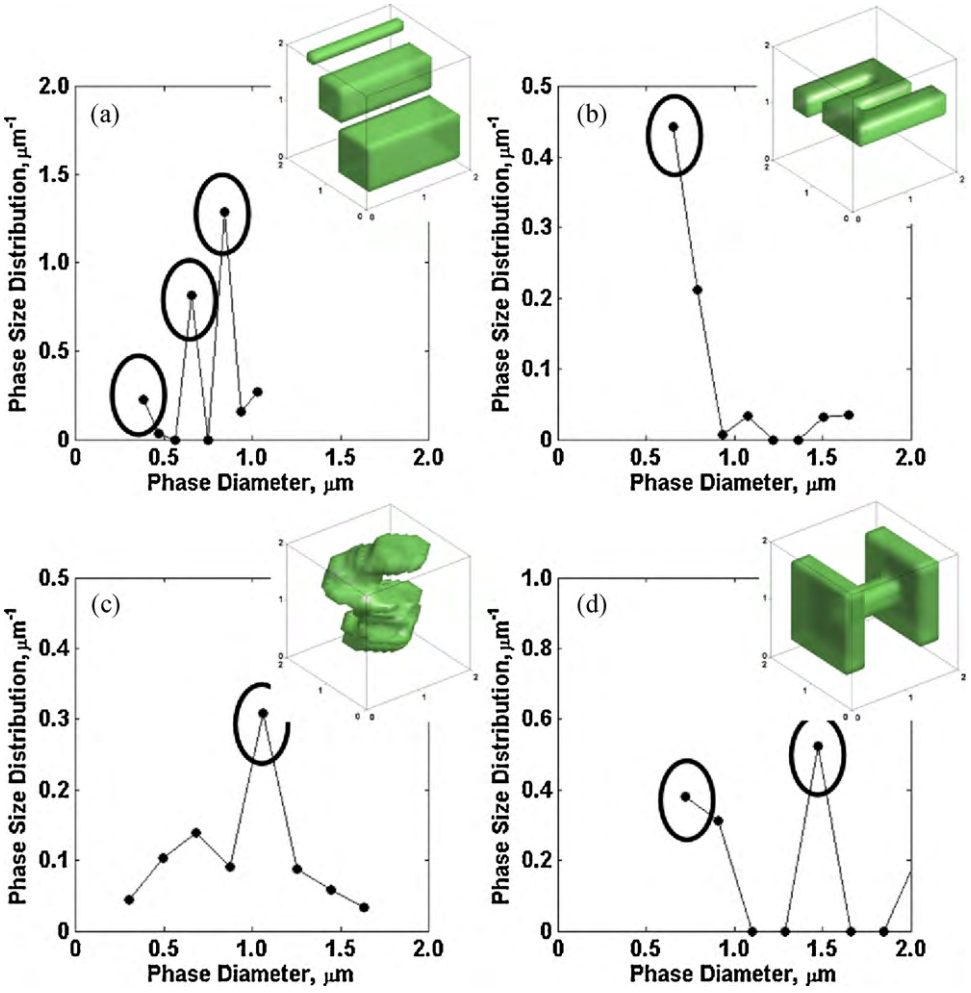

Fig. 2. The phase size distribution for four 20^3 voxel^3 test structures, (a–d), is shown. These structures are considered as 2^3 μm^3 structures (i.e., $\delta = 0.1$ μm). The primary cross-sectional diameters are circled. The trend lines are provided to guide the eye.

describe the data. This broadening is most pronounced in Fig. 2(c), which uses irregular cross-sections. These irregular cross-sections are responsible for the bumpy looking structure and secondary features at diameters surrounding the primary feature. These types of features, promoted by the voxel representation, can result in some noise in the analysis and in some statistical averaging of the primary features. These effects are anticipated and discussed in the theoretical development. Third, the tortuous structures have some anonymously large diameter contributions in the PSDs. This is evident in Fig. 2(b) and (c). These points are a result of several rays being shot down the "throat" of a phase path; in a direction parallel to the centerline. Likewise, in Fig. 2(d) a data point off of the figure exists. This feature has been suppressed because it is larger than the edge length of the volume itself. It is a result of the rays coming from the corners of the large square regions at the ends of the constricted regions. The rays coming from these types of features are an accepted product of the ray-shooting method.

The rays that have traveled down the throat of a phase path can be accounted for to some degree. In Eq. (4), it is recognized that N^{ϕ}_{Rays} rays can be expected for a phase path of diameter, D, which traverses the full sample. Large cross-section should have considerably more rays associated with an individual phase path than a small cross-section. Using the number that is anticipated for a full phase path of a discrete diameter, it can be used to build some intelligence into the interpretation of the tabulated ray-shooting data. A straight, square phase path with a cross-sectional diameter, D, should see approximately $4kD/\delta$ rays. This limit, or a similar variant, can be used to determine if there are a reasonable number of rays in a given histogram bin to represent at least one single phase path, or whether it may be reasonable to throw these rays out. Although there is some clear rationale to this approach, a straight phase path of constant diameter is most likely not a reasonable representation of a real heterogeneous structure. If localized regions of a larger cross-section exist within the structure, the associated rays could be improperly thrown out. Therefore, this approach is only provided as a point of discussion.

4.1.2. Grid dependence studies

The analysis of the test samples presented in Section 4.1.1, considers 8 histograms bins; however, it is important to have a methodology in place for the selection of the histogram bin density as we move to larger heterogeneous structures. The choice of the bin density is of importance to the independent repeatability of the phase size distributions. Several grid dependence studies are performed to provide insight.

We begin this discussion with the sphere-packing generated structures. A grid dependence study is provided for the sphere-packing generated structures in Fig. 3. The ray-shooting method is used to tabulate phase diameters for each phase of these individual structures. These tabulated diameters are consistently used throughout this study (i.e., for different grid densities). This data is unique to the structure and is used to populate histograms with increasing number of bins (e.g., 5, 10, 20, 30, 40, 50, etc.). As the number of bins that are populated by this tabulated data is increased, the mean phase diameter of the histogram and the normalization constant C^{*} (Eq. (11)) are calculated.

Using Eq. (11), the geometric normalization constants and the mean histogram phase diameter are shown in Fig. 3. There are two unique forms of the independent axis in Fig. 3: (i) the number of bins in the histogram and (ii) the differential bin diameter, ΔD. The differential bin diameter is calculated by dividing the difference between the maximum and minimum diameters tabulated using the ray-shooting method by the number of bins to be considered. It is not feasible to resolve differential diameters smaller than a single voxel; therefore, the minimum differential diameter is fixed for each analysis. The maximum number of bins that can be considered also has a practical limit. This limit corresponds to the maximum number of bins that can be used to between the maximum and minimum phase diameters identified by the ray-shooting method without using differential diameters smaller than the length of a single voxel. In Fig. 3, the practical limits for the respective independent axis are denoted with bold vertical lines. These lines are color coded to the appropriate trends for the sub-

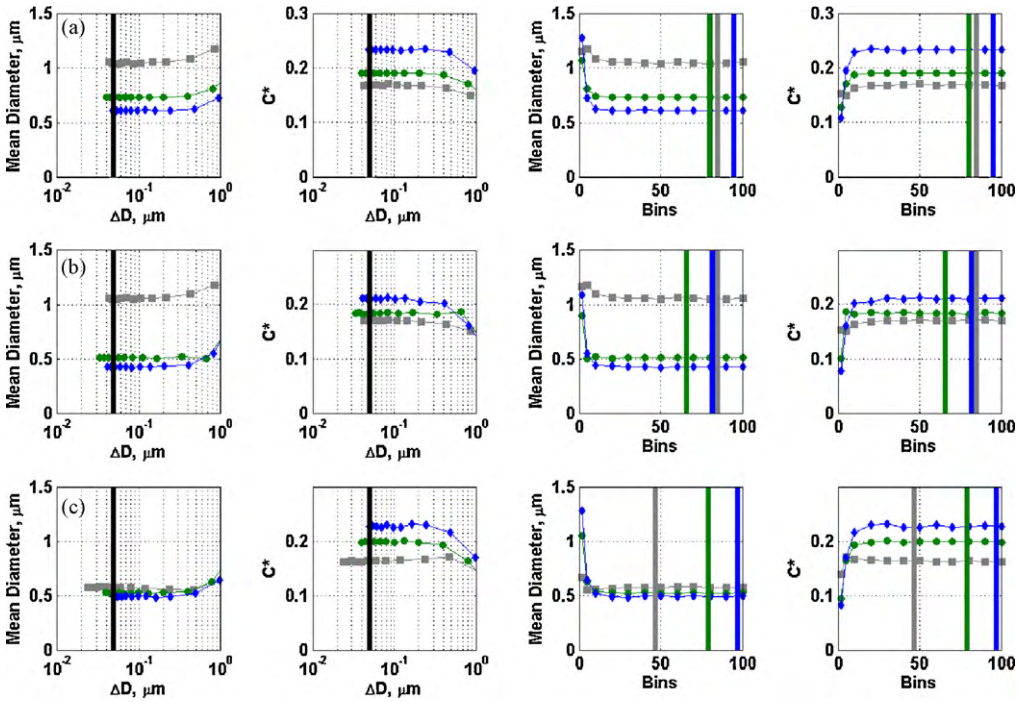

Fig. 3. The grid dependencies for the ray-shooting based phase size distribution method are examined for the sphere-packing generated structures with Ni and YSZ particle diameters of (a) Set 1: 1.0 and 1.0 μm, (b) Set 2: 1.0 and 0.5 μm, and (c) Set 3: 0.5 and 1.0 μm, respectively. The mean phase diameter of the histogram and the geometric constant, C^{*} (Eq. (11)) are examined as a function of the differential bin diameter, ΔD, and the corresponding number of bins which the ray-shooting method was broken down into to obtain this differential diameter, ΔD.

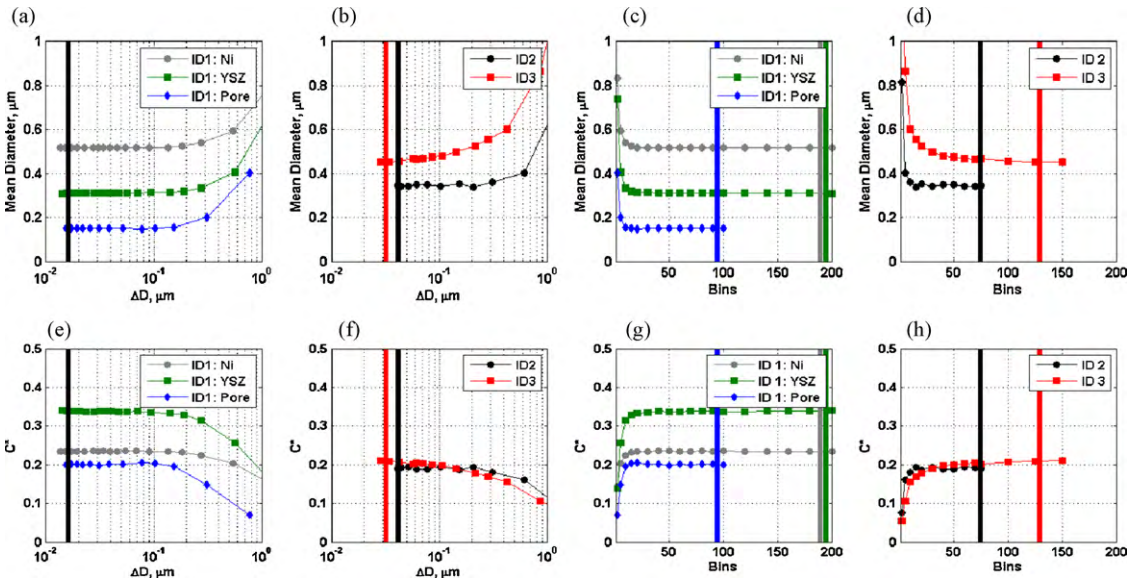

Fig. 4. The grid dependencies for the ray-shooting based phase size distribution method are provided in terms of the mean phase diameter of the histogram and the geometric constant, C^* (Eq. (11)). The dependence of the mean diameter of the histogram on differential bin diameter, ΔD, for (a) Sample ID 1 and (b) Samples ID 2 and ID 3; as well as dependence of the mean phase diameter calculated based upon the number of bins for (c) Sample ID 1 and (d) Samples ID 2 and ID 3. The geometric constant used for the normalization, C^*, as a function of the differential bin diameter, ΔD, for (e) Sample ID 1 and (f) Samples ID 2 and ID 3; and its dependence on the number of bins, for (g) Sample ID 1 and (h) Samples ID 2 and ID 3. The bold vertical lines indicate either the minimum differential diameter, ΔD, as dictated by the voxel size or the maximum numbers of discernable bins.

figures that use the number of histogram bins as the independent axis. A grid dependence study is also performed for Samples ID 1–3, which is provided in Fig. 4. The unique voxel resolution and number of voxels available, provides unique practical limits for these cases.

Several observations can be made regarding Figs. 3 and 4. First, the asymptotic behavior observed for each trend in Sets 1–3 in Fig. 3, as well as similar behavior for all three phases of Sample ID1 and the pore phase of Samples ID 2–3 in Fig. 4, demonstrates that grid independence for the PSD methods is achieved for all cases. Because the asymptotic behavior is observed prior to the practical limits for these trends, we have confidence that a consistent representation of the structure can be obtained. It also elucidates the importance of performing these types of studies, since grid independence can be reached at substantially different binning levels for different structures (e.g., independence at ~10 bins in Fig. 3 versus ~40 bins in Fig. 4).

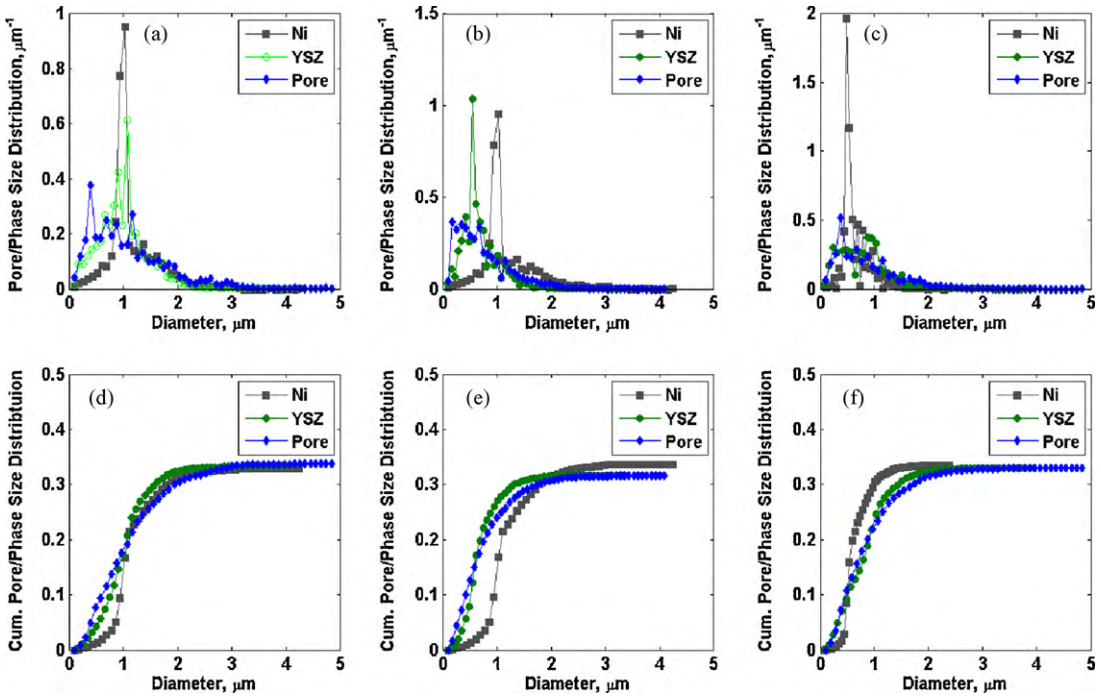

Fig. 5. The phase size distributions are provided for the sphere-packing generated structures with Ni and YSZ particle diameters of (a) Set 1: 1.0 and 1.0 μm, (b) Set 2: 1.0 and 0.5 μm, and (c) Set 3: 0.5 and 1.0 μm, respectively. Trend lines are provided to guide the eye. The corresponding cumulative phase size distributions for these structures (d) Set 1 (e) Set 2, and (f) Set 3, are also provided.

On the basis of the grid dependence studies, the numbers of bins used in the phase size distributions, or volume fraction distributions, are chosen in such a manner that the differential diameters considered were larger than the voxel length. In the generated structures, 50 bins are used so that a consistent number of bins could be considered and the selection corresponds to half the volume edge length for volumetric studies. In the samples reconstructed from XCT data, a differential diameter slightly less than twice the voxel length was chosen, due to the discrepancy in voxel size and resolution in the XCT imaged samples. This corresponds to approximately 75, 75, and 50 bins for the Ni, YSZ, and pore phases of Sample ID 1, respectively, 50 bins for Sample ID 2, and 75 bins for Sample ID 3. These selections are well within the region of grid independence. As a qualitative check, it is recognized that the geometric integration constant is comparable to the 1/4 noted in the theoretical development in Figs. 3 and 4. This provides further evidence of a successful implementation of the model.

4.1.3. Phase size distributions

With the histogram bin densities set, the phase size distributions for the generated structures are examined. In Fig. 5, the phase size distributions, as described by Eq. (12), are provided for the sphere-packing structures. Complementing the phase size distributions for these generated structures is a cumulative form of these same distributions, which represents the volume fraction of each phase contained in regions of diameter, D, and smaller.

An interesting observation is made regarding Fig. 5. In Fig. 5(a) and (d), which are measurements made on Set 1, there is a sharp peak for the Ni and YSZ phases at a diameter of approximately 1 μm. The Ni and YSZ phase size distributions of Set 2, shown in Fig. 5(b) and (e), have large contributions from diameters of 1 and 0.5 μm, respectively. Likewise, the Ni and YSZ phase size distributions of Set 3, shown in Fig. 5(c) and (f), have large contributions from diameters of 0.5 and 1 μm, respectively, with an additional YSZ peak at 0.5 μm. These observations are significant, because these diameters directly correspond to the constituent particle diameters used to generate these structures, which are provided in Table 1. The additional peak in the YSZ phase size distribution for Set 3 is believed to be a product of the Ni being permitted to overwrite the YSZ regions. The Ni in this set maintains a 0.5 μm diameter itself, and so this is likely similar phenomena to a harmonic subset.

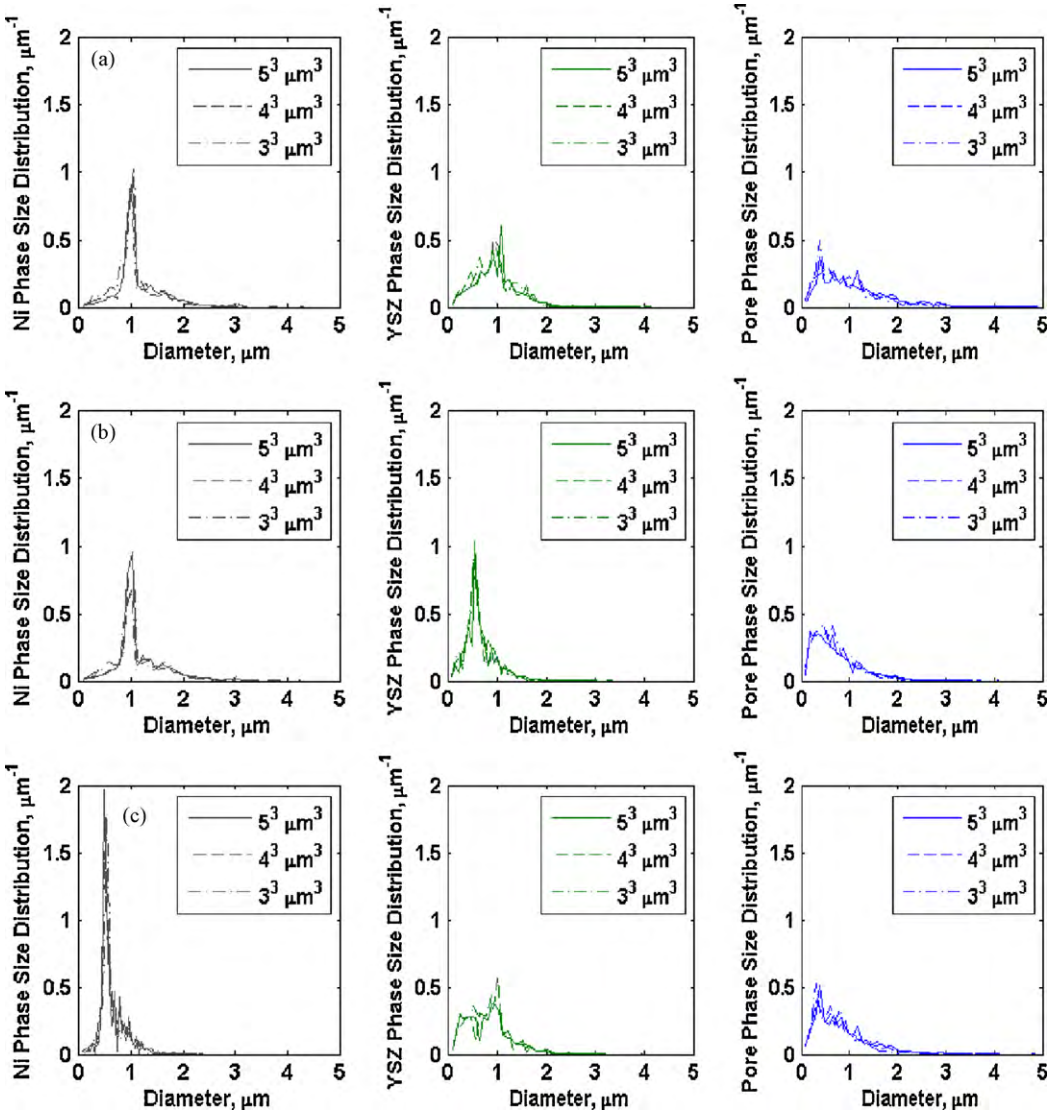

Fig. 6. The volumetric dependencies of the phase size distribution in 3^3, 4^3, and 5^3 μm^3 subsets of the sphere-packing generated structures. From left to right, the phase size distributions are shown for the Ni, YSZ, and pore regions, for the sets with Ni and YSZ particle diameters of (a) Set 1: 1.0 and 1.0 μm, (b) Set 2: 1.0 and 0.5 μm, and (c) Set 3: 0.5 and 1.0 μm, respectively. The data is actually discrete; trend lines are provided to guide the eye.

The primary Ni and YSZ particle diameters are reflected in the phase size distributions in Fig. 5; providing confidence in the method and the types of details that can be resolved. This can be taken as an additional qualitative check of the method. While the Ni and YSZ regions are generated using discrete particles, the pore space in all three generated structures was taken as those regions devoid of a Ni and/or YSZ particle. In Fig. 5, the pore space maintains a primary peak at approximately a 0.5 μm diameter in all three data sets. Secondary peaks are unique in all three data sets. The 0.5 μm diameter is a harmonic, or subset, of the constituent particle sizes used in all three generated structures. Without the use of discrete particles for the pore regions, the observation of harmonic subsets of the Ni and YSZ particle sizes is not unexpected. Finally, all three phases in all three data sets do exhibit some broadening. This is most pronounced with the void, or pore, regions which did not use discrete particles. As discussed with the test, or calibration, structures, this is expected. In a heterogeneous structure, such as these generated structures, this broadening can result not only from the discrete analysis as discussed with the test structures, but also from a range of diameters existing in the structure due to the overlap and over-writing of the constituent phases.

4.1.4. Effect of volumetric dependence on phase size distributions

As with our investigation of the heterogeneous samples in Part 1 [7], the effects of the sample volume considered to calculate the phase size distributions needs to be examined. This is intended to address the question of whether the phase size distribution developed is statistically representative of the structure, and if there is a volumetric dependence. To examine these details, some volumetric dependency studies are performed using the same sphere-packing structures. For this study, 3^3, 4^3, and 5^3 μm^3 subsets of these same generated volumes are repeatedly analyzed with the ray-shooting method. The phase size distributions from these volume subsets are provided in Fig. 6. In Fig. 6, the phase size distribution for the Ni, YSZ, and pore regions, respectively, are shown for the three sets of generated structures. To maintain a consistent basis for this analysis, the selection of the number of bins in the histogram was set to half the number of voxels along the edge of the cubic volume, $k/2$. If a volume smaller than the primary feature sizes were considered, there could be a substantial variation; however, is the consistent representation of the structure in all cases is noted.

This consistency is encouraging; however, a more quantitative measure is needed. The analysis of the phase size distributions is discrete with unique numbers of bins and bin-locations; therefore,

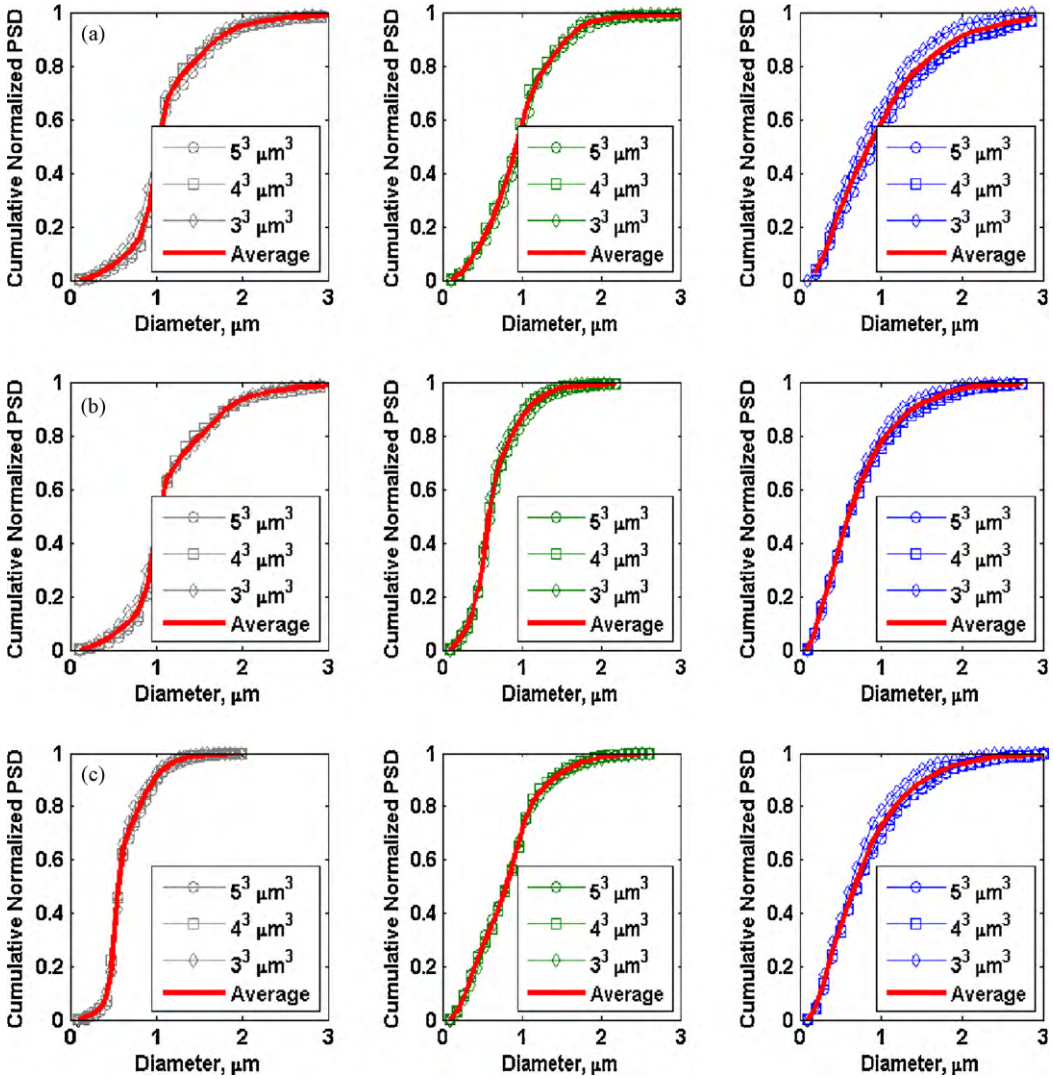

Fig. 7. The volumetric dependencies of a normalized form of the cumulative phase size distribution in 3^3, 4^3, and 5^3 μm^3 subsets of the sphere-packing generated structures. From left to right, the phase size distributions are shown for the Ni, YSZ, and pore regions, for the sets with Ni and YSZ particle diameters of (a) Set 1: 1.0 and 1.0 μm, (b) Set 2: 1.0 and 0.5 μm, and (c) Set 3: 0.5 and 1.0 μm, respectively. The average of the three trends is used for statistical analysis.

the discrepancies in the respective trends are not easily evaluated as a quantitative measure of error. Further, because the points are discrete, interpolation is not valid. To provide a quantitative measure of the effects of the volume considered, we revert to the cumulative PSD. By doing so, the trends become smooth and can be considered as piecewise continuous. With this representation of these cumulative phase size distributions, the data can be interpolated to a consistent grid and compared on a statistical basis. For this analysis, these cumulative phase size distributions are normalized as a fraction of the total phase volume so that the trends can be compared. This is done to negate any effects introduced due to differences in the volume fraction of the respective phases for the different volumes examined.

The cumulative phase size distributions for the 3^3, 4^3, and 5^3 μm^3 volumes, normalized to represent the fraction of the total volume subsumed by that phase, are provided in Fig. 7. The numeric average of the three individual data sets is also provided. Using this average, the error between the respective trends can be determined. The average error in the distributions is calculated,

$$\%\text{Error} = 100\% \frac{1}{M} \sum_{i=1}^{M} \frac{\max\left(\left|y(D_i) - \overline{y(D_i)}\right|\right)}{\overline{y(D_i)}} \quad (24)$$

where the value of a cumulative distribution, $y(D_i)$, and the average of the three cumulative distributions, $\overline{y(D_i)}$, are evaluated at each diameter of, D_i, for all M-bins. The mean percentage error from the average cumulative distribution for the Ni, YSZ, and pore regions of the sphere-packing structures are 11.2%, 4.1%, and 8.8%, respectively, for Ni and YSZ particles 1.0 μm in diameter (Set 1); 9.1%, 4.1%, and 3.2%, respectively for 1.0 μm Ni particles and 0.5 μm YSZ particles (Set 2); and 7.5%, 2.7%, and 5.5%, respectively, for 0.5 μm Ni particles and 1.0 μm YSZ particles (Set 3). This provides an average error for all three data sets of 6.2%. This agreement provides reasonable confidence in the consistent use of these methods for unique volume sizes.

4.1.5. Independent phase size distributions validation

The final point of validation that is provided is a comparison of diameters in Samples ID 2 and ID 3, as determined by the MIP and ray-shooting methods. This analysis is provided in Fig. 8, where the distributions are shown in their cumulative form so that they may be directly compared. In Fig. 8, two representations of the ray-shooting cumulative pore volume fraction are compared to that which is obtained from the MIP experiment Samples ID 2 and ID 3. For the ray-shooting data, (i) an unadulterated form and (ii) a form that considers a cutoff to filter the phase size distribution are considered. The cutoff forces the distribution to consider only data that contains at least the number of rays that would be required for a straight square pore of diameter, D, to traverse the sample volume. This cutoff is intended to remove volumes that can be associated with rays that have traversed the throats of the pores in the analysis and is formed on an intuitive foundation, as discussed in Section 4.1.1.

While agreement between the independent methods improved in Fig. 8 with the cutoff, it is recognized that the mismatch at large diameters is a product of the unique methods and assumptions. Specifically, as discussed with Fig. 6 of Part 1 [7], the MIP actually measures the throats of the pores. This tends to weight the pore-phase size distribution towards the smaller pore diameters and neglects the volumes attributed towards large diameters. This is the opposite of the ray-shooting methods, where the data is often weighted toward the larger phase diameters due to rays that have traveled down the throat of phase paths. The improved agreement with the cutoff applied to the ray-shooting results is indicative of this point.

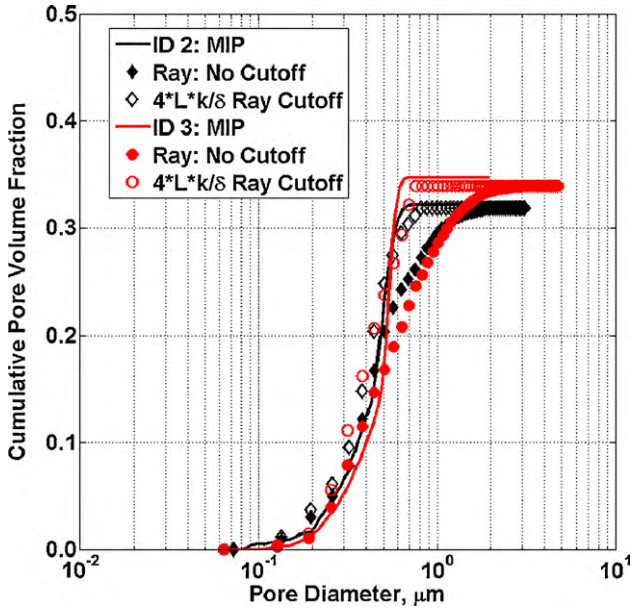

Fig. 8. The cumulative pore volume fraction is plotted versus pore diameter, D, as determined by the ray-shooting method and mercury intrusion porosimetry (MIP) for Samples ID 2 and ID 3. The ray-shooting cumulative pore volume fraction is shown for no cutoff (open symbols) and a $4kL/\delta$ ray cutoff (closed symbols).

Because the MIP and ray-shooting methods have been developed as unique but complementary interrogations of the structure with their own merits and limitations, this cutoff for the ray-shooting method is shown only for the sake of discussion and validation. Broader analysis and independent validation studies are necessary for examining the validity of such filtering type processes. As a result, all analysis presented in this and previous works that use similar ray-shooting methods do not use a cutoff methodology.

4.2. Transport phenomena

In the SOFC anode, the ionic, electronic, and mass transport processes occur in the YSZ, Ni, and pore regions, respectively. These processes are considered in the context of some test structures as well as the sphere-packing generated structures. A complete review of these results is not the purpose of this study. These studies are performed so that their results can be used in the proceeding section for the demonstration and validation of resistive loss distribution functions.

Table 2
Resistive losses observed in test structures.

Structure	Volume fraction	i, A cm^{-2}	Q''', W m^{-3}	Q, W
(a)	0.260	0.5	0.395×10^8	0.3×10^{-9}
		1.0	1.579×10^8	1.3×10^{-9}
		1.5	3.549×10^8	2.8×10^{-9}
		2.0	6.317×10^8	5.1×10^{-9}
(b)	0.099	0.5	2.547×10^8	2.0×10^{-9}
		1.0	10.189×10^8	8.2×10^{-9}
		1.5	22.929×10^8	18.3×10^{-9}
		2.0	40.799×10^8	32.6×10^{-9}
(c)	0.162	0.5	1.017×10^8	0.8×10^{-9}
		1.0	4.063×10^8	3.3×10^{-9}
		1.5	9.134×10^8	7.3×10^{-9}
		2.0	16.252×10^8	13.0×10^{-9}
(d)	0.265	0.5	1.143×10^8	0.9×10^{-9}
		1.0	4.573×10^8	3.7×10^{-9}
		1.5	10.298×10^8	8.2×10^{-9}
		2.0	18.314×10^8	14.7×10^{-9}

In lieu of a complete discussion on the results obtained from these studies, some specific notes, details, and implications of the cases considered are discussed. First, the four structures used to demonstrate the capabilities of the phase size distributions in Fig. 2 are used for similar purposes. These structures provide clean, conceptual structures, to test and examine the methods developed in the proceeding section. For these studies, the structures are considered as being comprised of YSZ at 1073 K with an ionic conductivity of 4.28 S m^{-1} [33]. Current densities of 0.5, 1.0, 1.5, and 2.0 A cm^{-2} are passed through the structures, which are applied as total fluxes. In other words, the Faradaic portion of the electrochemical oxidation process is neglected at this time. These cases can also be

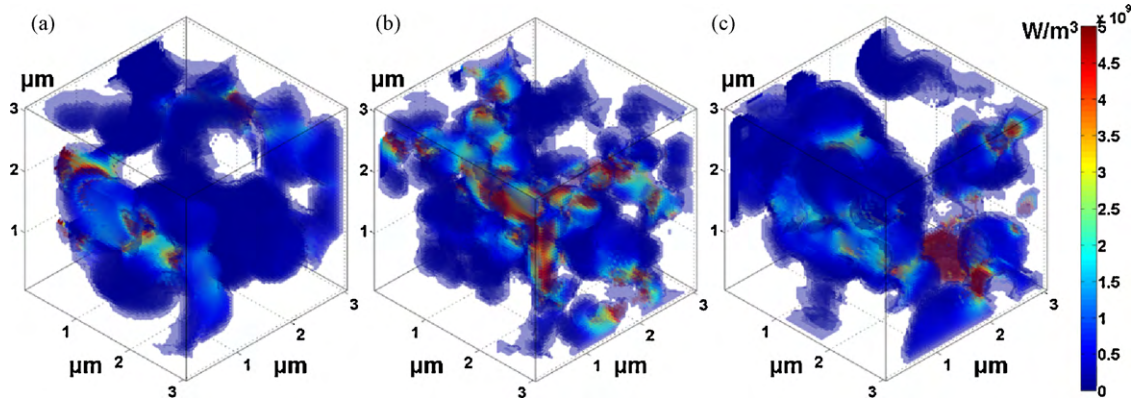

Fig. 9. The magnitude of the scalar resistive losses in the YSZ regions of a 3^3 μm^3 region of the sphere-packing structures at 1073 K and a current density of 1 A cm^{-2} for the sets with Ni and YSZ particle diameters of (a) Set 1: 1.0 and 1.0 μm, (b) Set 2: 1.0 and 0.5 μm, and (c) Set 3: 0.5 and 1.0 μm, respectively. The resistive losses are reported in W m^{-3} and maintain a consistent intensity scale.

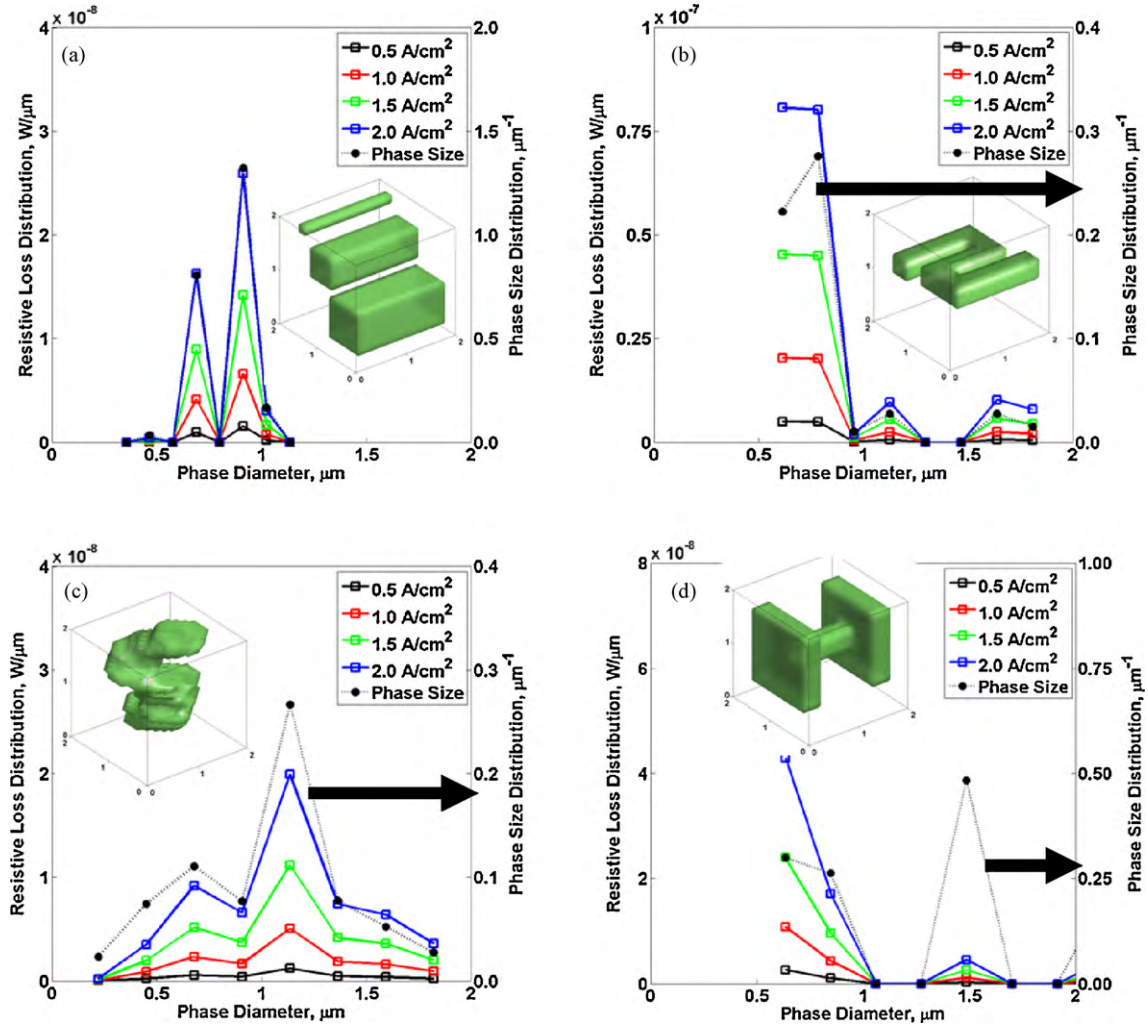

Fig. 10. The resistive loss distributions for the four test samples (a–d) are shown on the primary axis with the corresponding phase size distribution is reported on the secondary axis. The test structures are taken as YSZ at 1073 K, in a 2^3 μm^3 volume, with current densities of 0.5, 1.0, 1.5, and 2.0 A cm^{-2}. The trend lines are provided to guide the eye.

repeated for mass transport and electronic transport in the pore and Ni regions, respectively, but are inconsequential for the purposes of this demonstration. As with the phase size distribution analysis performed on these structures, they are considered as being 2 μm per edge, or 2^3 μm^3. The resistive losses of the structures in Fig. 2 are provided in Table 2. These results are used for the normalization and identification of the geometric constant used in the resistive loss distribution functions in Section 4.3.

A second set of transport studies are also performed on a 3^3 μm^3 subsets of the sphere-packing structures. These volumes are subjected to current densities of 1 A cm^{-2}. Again, the Faradaic portion of the electrochemical oxidation process is neglected. The mass transport and electronic charge transport can be considered; however, only those associated with the YSZ phase are reported here. This is done for consistency and due to the computational expense involved. The net resistive losses observed in these structures are 7.7×10^{-9}, 14.0×10^{-9}, and 9.1×10^{-9} W for the sphere-packing generated structures with Ni and YSZ particle diameters of, 1.0 and 1.0 μm, 1.0 and 0.5 μm, and 0.5 and 1.0 μm, respectively. These resistive losses were calculated by integrating the scalar volume-specific resistive losses over all of the phase volume within the structure. These regions have an YSZ volume fraction of 0.300, 0.271, and 0.325, respectively, providing volume-specific resistive losses of 2.728×10^8, 4.933×10^8, and 3.219×10^8 W m^{-3}, which were calculated by dividing the net resistive loss by the cube volume. For visualization purposes, the 3-D scalar resistive losses due to Joule heating in 3^3 μm^3 subsets of the YSZ regions of these three generated data sets are rendered in Fig. 9. Increased Joule heating is observed in constricted regions. These regions seem to occur where there is the partial overlap of two YSZ particles and/or partial obstruction from being overwritten with Ni.

4.3. Resistive loss and microstructure-induced resistive loss distributions

The extension of the methods that are used to examine the phase size distributions, to provide a quantitative measure of how these regions contribute to transport-related losses within the system, are examined in this discussion. The heat liberated due to Joule heating is examined in the context of the different phase diameters within the system. This approach can provide eventual insights as to how different microstructures contribute to polarization resistances, the effects of microstructural degradation on transport-related losses, and potential sources of degradation.

4.3.1. Resistive loss distribution in test structures

We begin this study by examining the same test structures that were considered during the development of the phase size distributions, which are rendered in Fig. 2. As discussed in Section 4.2, these structures were subjected to an ionic current density of 0.5, 1.0, 1.5, and 2.0 A cm^{-2}, where the rendered regions were considered as being comprised of YSZ at 1073 K. The net resistive losses

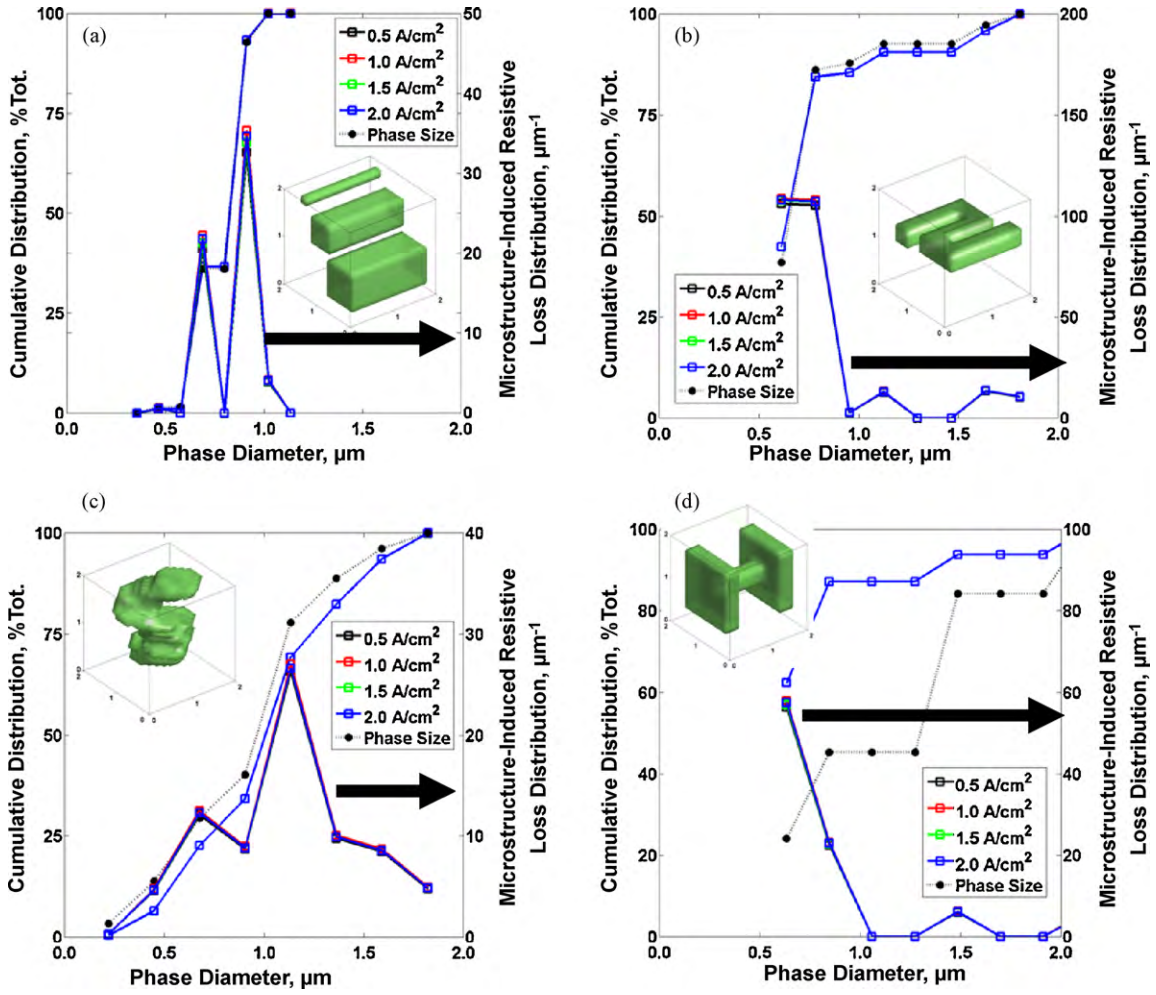

Fig. 11. The cumulative resistive loss and cumulative phase size distributions for four test samples (a–d) are provided on the primary axis. The microstructure-induced resistive loss distribution is shown on the secondary axis. These test structures are taken as YSZ at 1073 K, in a 2^3 μm^3 volume, with current densities of 0.5, 1.0, 1.5, and 2.0 A cm^{-2}. The trend lines are provided to guide the eye.

for these cases are provided in Table 2. In Fig. 10, the resistive loss distributions and phase size distributions are shown for these cases. The resistive loss distribution is shown on the primary axis and the phase size distribution on the secondary axis. The magnitude of the resistive loss distribution increases with increasing current density. It is interesting to note that for Fig. 10(a)–(c), these resistive loss distributions follow the phase size distributions quite well. This implies that the phase diameters contributing to the largest volumes within these structures are also responsible for the largest contributions of Joule heating. This is not unexpected, as the current passes through discrete regions with controlled structure. These structures have consistent cross-sections and are without constriction. The net current carried by a given region is proportional to its cross-section.

Moving to Fig. 10(d), the resistive loss distribution does not directly follow the phase size distribution. Rather, most of the net resistive losses are found to be attributed to the smaller phase diameters. These resistive losses are specifically attributed to the constricted region, despite the much smaller volume attributed to this region. The rationale for this occurrence is that the current being forced through this constriction results in resistive losses due to Joule heating that outweigh the impact of the region's smaller volume. As expected, this effect is amplified with increasing current density due to Joule heating losses scaling with the square of the magnitude of the current density.

4.3.2. Microstructure-induced resistive loss distribution in test structures

In the preceding section, the resistive loss distributions are dependent upon the operating conditions. The applied current density, as well as factors such as the material's resistivity, can result in unique trends. This makes it difficult to extract the underlying effect of the microstructure on the transport processes. The microstructure-induced resistive loss distribution was developed to negate these discrepancies so that independent materials and operating conditions can directly be compared on a consistent basis. This provides a means of quantifying the effects of the microstructure on transport-related losses such that they are a property of the microstructure and not the specific model parameters or case.

Using the same test structures that have been used throughout this manuscript, Fig. 11 provides both the normalized cumulative resistive loss distribution, as well as normalized cumulative phase size distribution, on the primary axis. The microstructure-

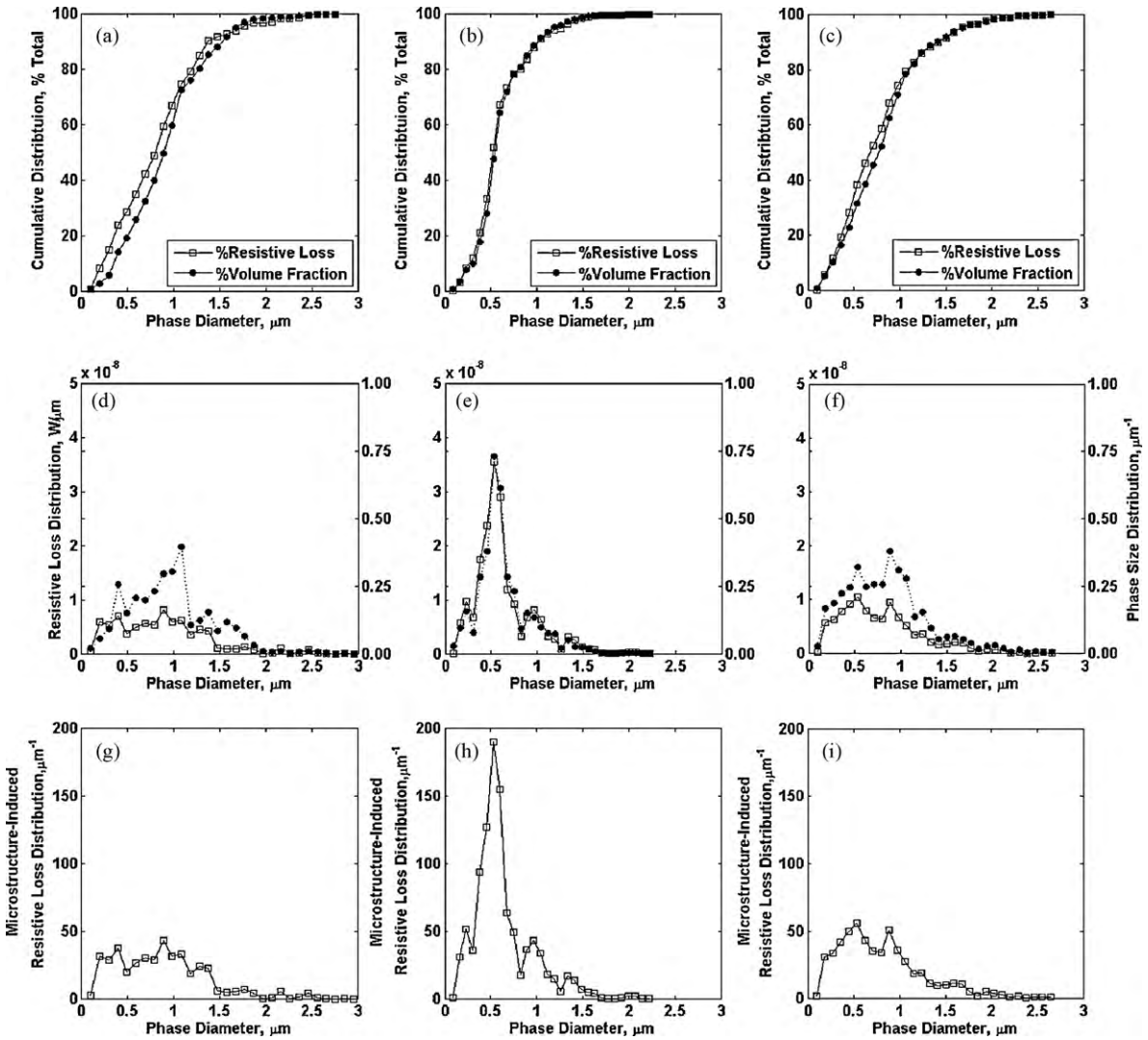

Fig. 12. The normalized cumulative phase size (closed symbol) and resistive loss distributions (open symbols) in a 3^3 μm^3 YSZ region of the sphere-packing structures with Ni and YSZ particle diameters of (a) Set 1: 1.0 and 1.0 μm, (b) Set 2: 1.0 and 0.5 μm, and (c) Set 3: 0.5 and 1.0 μm, respectively. The resistive loss distributions (open symbols) for these structures are provided on the primary axis of (d) Set 1, (e), Set 2, and (f) Set 3, with the phase size distribution (closed symbol) on the secondary axis. The microstructure-induced resistive loss distributions are provided for (g) Set 1, (h) Set 2, and (i) Set 3.

induced resistive loss distribution is provided on the secondary axis. The normalized cumulative distributions represent the percentage of the respective distributions attributed to regions of a phase diameter, D, and smaller. The microstructure-induced resistive loss distributions are calculated using Eq. (23).

Several observations can be made regarding Fig. 11. First, the microstructure-induced resistive loss distributions have collapsed on top of each other for each unique current density. This confirms that the normalization used to create this distribution function makes this distribution a function of the microstructural details. Second, the normalized cumulative phase size distribution and the normalized cumulative resistive loss distributions correlate quite well in Fig. 11(a)–(c), but not so for Fig. 11(d). This observation in Fig. 11(d), again points to the effect of the constricted region maintaining resistive losses that outweighs its volumetric contribution.

4.3.3. Sphere-packing generated structures

To demonstrate the effects of the resistive loss distributions and microstructure-induced resistive loss distributions, $3^3\ \mu m^3$ subsets of the sphere-packing generated volumes are examined. The YSZ regions are subjected to a $1\ A\,cm^{-2}$ current density at 1073 K. The phase size distribution, resistive loss distribution, microstructure-induced resistive loss distribution, and the corresponding normalized cumulative phase size and resistive loss distributions are examined. These results are presented in Fig. 12. As with the volumetric dependency studies for the phase size distribution analysis, $k/2$ bins are used in this study. Because the $3^3\ \mu m^3$ volume contains 61^3 voxels, data populates 30 bins for the phase size distribution and the resistive loss distribution analyses.

There are a number of observations that can be regarding Fig. 12. We begin by examining the normalized cumulative phase size distribution and the normalized cumulative resistive loss distribution, where both are plotted as a percentage of their total for regions of phase diameter, D, and smaller. In Fig. 12(a)–(c), these forms of the cumulative distribution are shown for the three sets of sphere-packing generated structures, respectively. The two trends correlate reasonably well in each of these sub-figures. This suggests that the contributions within the structure from volumetric and microstructural effects (e.g., constrictions) are of comparable magnitude and/or volumetrically dominated.

Moving to the resistive loss distributions in Fig. 12(d)–(f), which are shown on the primary axis with the phase size distribution on the secondary axis, the unique properties of the same respective studies can be examined. The correlation between the two trends is again noted in each of the sub-figures. The most significant discrepancies occur in Fig. 12(d) and (f). These figures correspond to Sets 1 and 3, which are the cases that considered 1.0 μm diameter YSZ particles. This is opposed to Fig. 12(e), which corresponds to Set 2 and maintains 0.5 μm YSZ particles. The primary source of these discrepancies is recognized at smaller to mid-range phase diameters. This may seem surprising because, while these regions have a smaller volume, they are often attributed to regions of constriction that result in increased Joule heating. However, Set 2 maintains the smallest YSZ particles and also has the largest resistive losses. Further, the broader phase size distributions of Sets 1 and 3 in Fig. 12(d) and (f), respectively, suggest that there is less volume in these data sets attributed to these smaller diameter regions.

Examining Fig. 12(g)–(i), the microstructure-induced resistive loss distribution is shown for the same respective cases. Again, the broad effects of the microstructure are highlighted in Fig. 12(g) and (i), while the microstructure had a considerable impact on Set 2 in Fig. 12(h), which considered the 0.5 μm YSZ particles. This effect is approximately 4× that in the other two sets. This is most likely the result of the increased probability and volume attributed to regions of constricted cross-section. These regions can result from the smaller constituent particles and are exemplified by the phase size distribution maintaining its primary volumetric peak at this 0.5 μm YSZ particle diameter, which also corresponds to the large microstructure-induced resistive loss distribution peak.

5. Conclusions

Several qualitative and quantitative measures of a heterogeneous structure and its effect on transport-related processes are introduced in this work. Specifically, the details surrounding methods developed by the authors' to examine these properties are discussed, demonstrated, and verified. Test structures, sphere-packing generated structures, and several XCT imaged SOFC electrode samples are considered. All of the methods discussed in this work are developed for the purpose of examining 3-D non-destructively imaged segments of an SOFC anode microstructure; however, they may find application with other characterization methods or communities. The methods discussed in this work can assist in understanding the details of a heterogeneous structure and how it impacts attributed transport processes.

Within this discussion, the phase size distributions of the various samples and structures are discussed, which are determined using a ray-shooting method. This approach has been developed using a lattice Boltzmann based spatial discretization method. The ray-shooting method is used with an analytic development to produce a histogram that represents the portion of the volume fraction of given phase within the structure attributed to a phase diameter, D, within a differential diameter. This method was then adapted so that it could concurrently examine a complementary structure containing scalar resistive loss values, due to Joule heating, within the structure. The scalar resistive loss distributions required independent, but complementary, development. This distribution also required an independent, detailed transport analysis to identify the transport-related losses in the system. This analysis has been shown to be able to describe the combination of the microstructural (e.g., constrictions) and volumetric contributions to the irreversibility in SOFC anode transport processes.

Acknowledgments

The authors gratefully acknowledge financial support from the Army Research Office Young Investigator Program (Award 46964-CH-YIP), the National Science Foundation (Award CBET-0828612), an Energy Frontier Research Center on Science Based Nano-Structure Design and Synthesis of Heterogeneous Functional Materials for Energy Systems funded by the U.S. Department of Energy, Office of Science, Office of Basic Energy Sciences (Award DE-SC0001061) and the ASEE National Defense Science and Engineering Graduate Fellowship program. The authors also acknowledge the use of the Advanced Photon Source supported by the U.S. Department of Energy, Office of Science, Office of Basic Energy Sciences, under contract No. DE-AC02-06CH11357. Additional thanks go to Adaptive Materials, Inc. for providing SOFC samples, Dr. Yong S. Chu (Brookhaven National Laboratory) for his help with the experimental efforts, Dr. Abhijit S. Joshi (Drexel University) for his contributions to the LBM ray-shooting discretization as well as discussions on the LBM based transport studies, and Prof. George J. Nelson (University of Connecticut) for proofreading the manuscript.

References

[1] K.N. Grew, Y.S. Chu, Y. Jaemock, A.A. Peracchio, J.R. Izzo Jr., Y. Hwu, F. De Carlo, W.K.S. Chiu, J. Electrochem. Soc. 157 (6) (2010) B783–B792.
[2] J.R. Izzo Jr., A.S. Joshi, K.N. Grew, W.K.S. Chiu, A. Tkachuk, S.H. Wang, W. Yun, J. Electrochem. Soc. 155 (5) (2008) B504–B508.
[3] J.R. Wilson, W. Kobsiriphat, R. Mendoza, H.-Y. Chen, J.M. Hiller, D.J. Miller, K. Thornton, P.W. Voorhees, S.B. Adler, S.A. Barnett, Nat. Mater. 5 (7) (2006) 541–544.

[4] J.R. Wilson, S.A. Barnett, Electrochem. Solid State Lett. 11 (10) (2008) B181–B185.
[5] D. Gostovic, J.R. Smith, D.P. Kundinger, K.S. Jones, E.D. Wachsman, Electrochem. Solid State Lett. 10 (12) (2007) B214–B217.
[6] P.R. Shearing, J. Golbert, R.J. Chater, N.P. Brandon, Chem. Eng. Sci. 64 (17) (2009) 3928–3933.
[7] K.N. Grew, A.A. Peracchio, A.S. Joshi, J.R. Izzo Jr., W.K.S. Chiu, J. Power Sources 195 (24) (2010) 7930–7942.
[8] J.B. Goodenough, H.D. Abruna, M.V. Buchana, S. Visco, M. Stanley, B. Dunn, Y. Gogotsi, A. Gewirth, D. Nocera, Basic Research Needs for Electrical Energy Storage: Report of the Basic Energy Sciences Workshop on Electrical Energy Storage, U.S. Department of Energy, 2007.
[9] K.N. Grew, A.A. Peracchio, J.R. Izzo Jr., W.K.S. Chiu, ECS Trans. 25 (2) (2009) 1861–1870.
[10] A.S. Joshi, K.N. Grew, J.R. Izzo Jr., A.A. Peracchio, W.K.S. Chiu, ASME J. Fuel Cell Sci. Technol. 7 (1) (2010) 011006.
[11] A. Tkachuk, F. Duewer, H. Cui, M. Feser, S. Wang, W. Yun, Z. Kristallogr. 222 (11) (2007) 650–655.
[12] M. Feser, J. Gelb, H. Chang, H. Cui, F. Duewer, S.H. Lau, A. Tkachuk, W. Yun, Meas. Sci. Technol. 19 (9) (2008) 094001.
[13] Y.S. Chu, J.M. Yi, F. De Carlo, Q. Shen, W.-K. Lee, H.J. Wu, C.L. Wang, J.Y. Wang, C.J. Liu, C.H. Wang, S.R. Wu, C.C. Chien, Y. Hwu, A. Tkachuk, W. Yun, M. Feser, K.S. Liang, C.S. Yang, J.H. Je, G. Margaritondo, Appl. Phys. Lett. 92 (10) (2008) 103119.
[14] Y.-T. Chen, T.-N. Lo, Y.S. Chu, J. Yi, C.-J. Liu, J.-Y. Wang, C.-L. Wang, C.-W. Chiu, T.-E. Hua, Y. Hwu, Q. Shen, G.-C. Yin, K.S. Liang, H.-M. Lin, J.H. Je, G. Margaritondo, Nanotechnology 19 (39) (2008), 395302.
[15] D. D'Humières, I. Ginzburg, M. Krafczyk, P. Lallemand, L.-S. Luo, Philos. Trans. R. Soc. A 360 (2002) 437–451.
[16] R.S. Maier, R.S. Bernard, D.W. Grunau, Phys. Fluids 8 (7) (1996) 1788–1801.
[17] Y.H. Qian, D. d'Humières, P. Lallemand, J. Stat. Phys. 68 (3–4) (1992) 563–573.
[18] P. Asinari, M.C. Quaglia, M.R. von Spakovsky, B.V. Kasula, J. Power Sources 170 (2) (2007) 359–375.
[19] M.C. Sukop, D.T. Thorne, Lattice Boltzmann Modeling, Springer, Berlin, 2006.
[20] S. Succi, The Lattice Boltzmann Equation for Fluid Dynamics and Beyond, Oxford University Press, Oxford, 2001.
[21] X. He, L.-S. Luo, Phys. Rev. E 55 (6 Suppl. A) (1997) R6333–R6336.
[22] X. He, L.-S. Luo, Phys. Rev. E 56 (6) (1997) 6811–6817.
[23] X. He, L.-S. Luo, J. Stat. Phys. 88 (3–4) (1997) 927–944.
[24] L.-S. Luo, S.S. Girimaji, Phys. Rev. E 67 (3 2) (2003) 036302.
[25] M.E. McCracken, J. Abraham, Phys. Rev. E 71 (4) (2005).
[26] D.A. Bader, Petascale Computing: Algorithms and Applications, Chapman & Hall, Boca Raton, 2008.
[27] A.S. Joshi, A.A. Peracchio, K.N. Grew, W.K.S. Chiu, J. Phys. D 40 (9) (2007) 2961–2971.
[28] S. Chen, G.D. Doolen, Ann. Rev. Fluid Mech. 30 (1998) 329–364.
[29] X. Shan, G. Doolen, Phys. Rev. E 54 (4 Suppl. A) (1996) 3614–3620.
[30] A.S. Joshi, A.A. Peracchio, K.N. Grew, W.K.S. Chiu, J. Phys. D 40 (23) (2007) 7593–7600.
[31] A.S. Joshi, K.N. Grew, A.A. Peracchio, W.K.S. Chiu, J. Power Sources 164 (2) (2007) 631–638.
[32] Q. Zou, X. He, Phys. Fluids 9 (6) (1997) 1591–1596.
[33] K. Sasaki, J. Maier, Solid State Ionics 134 (3–4) (2000) 303–321.